EXPERIMENTAL FLOWFIELD AND AEROACOUSTIC INVESTIGATION OF TWIN ROTORS IN HOVER CONDITIONS

Fabrizio De Gregorio, Italian Aerospace Research Centre - CIRA, Capua, Italy
Paolo Candeloro, University Niccolò Cusano, Roma, Italy
Fabio Del Duchetto, University Niccolò Cusano, Roma, Italy
Tiziano Pagliaroli, University Niccolò Cusano, Roma, Italy

Abstract

The study examined the acoustic and aerodynamic properties of small rotors, considering the impact of rotor-rotor interactions. Two rotors equipped with three-bladed propellers, each with a diameter of 393.7 mm, were tested at a fixed rotational speed of 5200 RPM, with various configurations in terms of phase delay and mutual distance between the rotors. The aerodynamic loads, flow field velocity, and acoustic emissions were analysed using a six-component load cell, Particle Image Velocimetry, and microphone array measurements. The aerodynamic characteristics of the individual rotor were assessed across different rotational speeds. Additionally, the interaction between the rotor slipstreams for side-by-side rotors was investigated under co-rotating and counter-rotating configurations at distances between the rotor axes of 1.02D, 1.1D, and 1.2D. The findings indicated that the slipstreams of the side-by-side rotors deflect and change with the inter-axial distance, with the rotor-rotor interaction and acoustic emissions being influenced by the rotor distance. A noticeable decrease in thrust was observed at the closest distance of 1.02D. Regarding acoustic emissions, the overall sound pressure level increased when the rotors operated in counter-rotating verses compared to the co-rotating case.

1 NOMENCLATURE

Symbol	Description	Units
c	Chord length	m
d	Rotor interaxial distance	m
D	Rotor diameter	m
r	Local radius	m
R	Rotor radius	m
t	Blade thickness	m
V_{Tip}	Blade tip speed ($=\Omega R$)	m/s
u, v, w	Velocity components	m/s
x, y, z	Geometrical coordinates	m
$\Delta x, \Delta y$	Space resolution	mm
β	Blade twist	deg
σ	Rotor solidity	
ω_y	Out-of-plane vorticity	$1/s$
θ	Blade azimuth angle	deg
ψ	Phase angle	deg
Ω	Rotor speed	RPM

2 INTRODUCTION

The development of aerial vehicles for Urban Air Mobility (UAM) aims to address congestion issues in city transportation. This has prompted research into the aerodynamic and acoustic characteristics of these vehicles (Ref. 1, Ref. 2). Multirotor propulsion systems are increasingly being utilized in Vertical Take-Off and Landing (VTOL) configurations, particularly for small-scale drones used in surveillance, monitoring, search and rescue, aerial surveying, and photography.

Rotor slipstreams are characterized by strong vortices that form and trail from each blade. These flow structures have been extensively studied in the development of rotorcraft vehicles (see among many Ref. 3 and Ref. 4). If the study of classic rotorcraft configurations foresees the presence of one or at most two rotors, the novel VTOL UAM configurations foresee a minimum of 4-8 rotors, which could increase in the case of distributed electric propulsion. In addition, the ranges of the flow regimes are substantially different: helicopters typically fly at Reynolds numbers O (10^6) whereas multirotor drones, which are equipped with blades of smaller sizes, operate at Reynolds numbers O (10^4 – 10^5).

The placement of rotors in a side-by-side or tandem configuration offers valuable insights into the aerodynamics and acoustics of multirotor setups. In recent years have seen several experimental and numerical investigations focused on tandem configurations.

Sinibaldi and Marino (Ref. 5) conducted an experimental analysis of the aeroacoustic characteristics of a propeller designed for small multirotor UAV propulsion.

In a study conducted by Intaratep et al. (Ref. 6), the noise and thrust performance of small UAVs were measured. The study examined how the number of rotors in a quadcopter affects its sound. It found that quadcopters with 4 rotors produce dominant tones at specific frequencies up to 6000 Hz, while smaller rotors only slightly change the sound at mid and high frequencies. The number of rotors (1, 2, or 4) doesn't significantly affect the sound signature, but there is a noticeable increase in overall noise when moving from 2 non-adjacent rotors to 4 rotors. Additionally, for small-scale drones, rotor configuration greatly influences thrust performance.

Zhou et al. (ref. 7) discovered that the separation distance had a minimal effect on the rotor's thrust coefficient, with a variation of less than 2% for all test cases. However, they observed a significant increase in thrust fluctuations (thrust standard deviation) as the separation distance decreased. Additionally, tonal and broadband noise increased as the axial distance decreased.

Shukla and Komerath (Ref. 8) investigated the aerodynamic and the flow field characteristics of a set of side-by-side rotors. The instantaneous and time-averaged S-PIV data indicated an increase in inter-rotor wake interactions with decreased rotor spacing and Reynolds number. A reduction in rotor efficiency was observed at small rotor spacing at low Reynolds numbers through thrust and torque measurements. The flow field measurements revealed substantial interactions between the rotors, leading to distortion, loss of coherence, and deviation from typical trajectories of the wake features as a result of minor axis shifts.

Chen et al. (Ref. 9) investigated several multirotor configurations, the rotor interaction depicted a thrust loss of 5% for a distance of 1.025 the rotor diameter. They also claimed that the loss of thrust was influenced by disk loading, and the more loaded the propeller was, the greater the loss of thrust.

Lee and Lee (Ref. 10) performed a numerical simulation of a quadcopter under hover flight conditions to investigate the mutual rotor-to-rotor interactional effects on the aerodynamic performance, wake structures, and sound pressure level using the nonlinear vortex lattice method with the vortex particle method and acoustic analogy based on Farassat's formulation 1A. Results showed that the average thrust force decreases significantly and force fluctuation is found to increase dramatically as the rotor spacing gets smaller. In addition, the wake geometry and induced flow structure behind the rotor tended to be radially dragged down toward the centre of the vehicle due to the existence of the adjoining rotor, which consequently resulted in strong wake-to-wake interaction and the formation of asymmetric wake structures although the multirotor operates under the hovering condition. It was also observed that unsteady loading introduced by rotor interaction leads to a considerable increase in the sound pressure level, particularly the normal direction of the rotor plane.

In the given context, the GARTEUR Action Group HC/AG-26 (Ref. 11) was established to advance the current understanding of rotor interaction. The project team comprises 14 partners coordinated by DLR. The primary objectives of this working group are twofold. Firstly, to expand the knowledge on the generation and transmission of noise from multirotor systems, while considering installation effects. Secondly, to develop and validate numerical methods for predicting noise emitted by multirotor systems. The partner shares test results for code validation among all participants. Three test databases were available, which are from DLR (Ref. 12), CIRA/ University Niccolò Cusano (Ref.13) and PoliMi (Ref.14) and new ones were planned. Preliminary comparisons between numerical predictions and experimental data have been documented by Yin et al. (Ref. 16).

Accordingly, CIRA and University Niccolò Cusano carried out two distinct measurement campaigns, one aimed at the aerodynamic and fluid-dynamics characterization of the rotor mutual interaction and one for studying its acoustic emissions. The measurements were conducted at the CIRA Aerodynamic and the semi-anechoic chamber. For the sake of clarity, we want to specify that the measurements were not carried out simultaneously to avoid any possible contamination of the acoustic chamber by the seeding material used for the PIV measurements.

The rotor wake interaction effect was investigated on a three-bladed twin rotor test rig. The effect on the aerodynamic and acoustic emissions was studied by varying the rotor axial distance and by the rotating versus.

The paper illustrates the experimental activities carried out during the two different test campaigns. The activity aims to characterize the multi-rotor system in terms of loads, velocity fields and acoustic emissions. The first part of the paper describes the main characteristics of the multi-rotor test rig, the experimental setup, the different rotor configurations and the selected test matrix. The study ends with the results related to the ensemble average velocity fields for isolated rotor and tandem configurations, together with the load measurements concerning the effects of the propeller interaction on the aerodynamic efficiency. The multi-rotor wake interaction is then discussed in terms of acoustic emission looking for possible relations between the different physical magnitudes.

3 EXPERIMENTAL SETUP

3.1 Rotor Rig

The test rig was designed to investigate the interaction effect of a multirotor in a twin configuration allowing the variation of the inter-axis distance (Figure 1). Each rotor was driven by a KDE4012XF-400 brushless motor with a dedicated electronic speed controller (ESC) model KDEXF-UAS55.

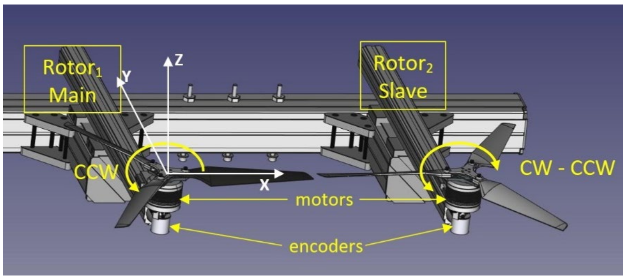

Figure 1: Rotor test rig

A custom control system was implemented in LabView environment to set the rotor speed and the relative positions using an NI PXI-1031 with motion controller NI-PXI-7350 and multifunction DAQ NI PXI-6259. The rotor rotational speed and blade relative positions were measured using a Kubler 05.2400 incremental encoder with 500 pulses per revolution (PPR). The main rotor, also named rotor1, rotates counterclockwise for all the test campaigns, and the slave rotor, or rotor2, runs counterclockwise and clockwise according to the corotating or counter-rotating configuration. The relative phase angle ψ between the two propellers is defined in Figure 2.

The twin rotors were placed at three different reciprocal distances at d_1 = 1.02 D, d_2 = 1.1 D and d_3 = 1.2 D, where D is the rotor diameter. The twin rotors were operated in hover conditions at constant rotor speed Ω = 5200 RPM. The rotors were equipped with three-bladed propellers, type KDE-CF155-TP (15.5” x 5.3”). The rotors had a diameter of D = 393.7 mm and a chord of c = 28.5 mm.

The twin rotors were placed at three different reciprocal distances at d_1 = 1.02 D, d_2 = 1.1 D and d_3 = 1.2 D, where D is the rotor diameter. The twin rotors were operated in hover conditions at fixed rotor speed Ω = 5200 RPM. The rotors were equipped with three-bladed propellers, type KDE-CF155-TP (15.5” x 5.3”). The rotors had a diameter of D = 393.7 mm and a chord of c = 28.5 mm.

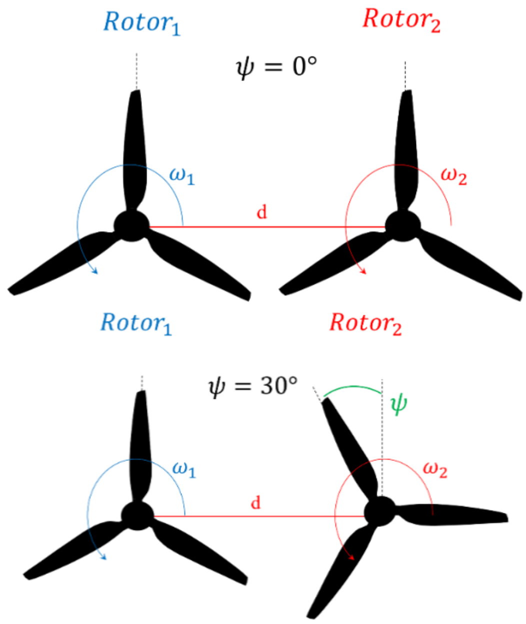

Figure 2: Definition of the phase angle between the propellers.

The rotors were equipped with three-bladed propellers, type KDE-CF155-TP (15.5” x 5.3”). The rotors had a diameter of D = 393.7 mm and a chord of c = 28.5 mm. Considering that the propeller blade is tapered and swept, c is referred to as the mean aerodynamic chord (MAC). The resulting rotor solidity value was equal to σ = 0.138. The rotor solidity is defined as $\sigma = BcR/A = Bc/\pi R$ where B is the number of the blades of the rotor, c is the mean aerodynamic chord, R is the radius of the rotor, and A is the rotor disk area. The commercial blade geometry was measured by an Exagon scanner laser, model 8525-7 with a spatial resolution of 0.048 mm. The blade is depicted in Figure 3-a together with several airfoils equispaced each of 10 mm. The geometry details in terms of normalised chord, normalised thickness and twist distribution along the radius are given in Figure 3-b.

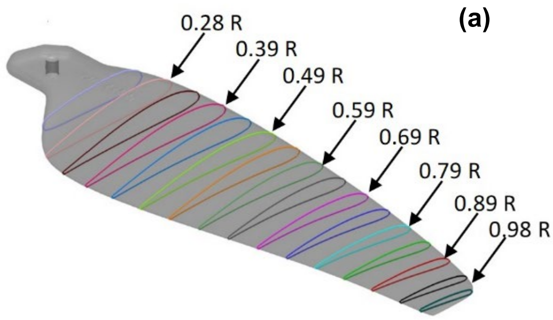

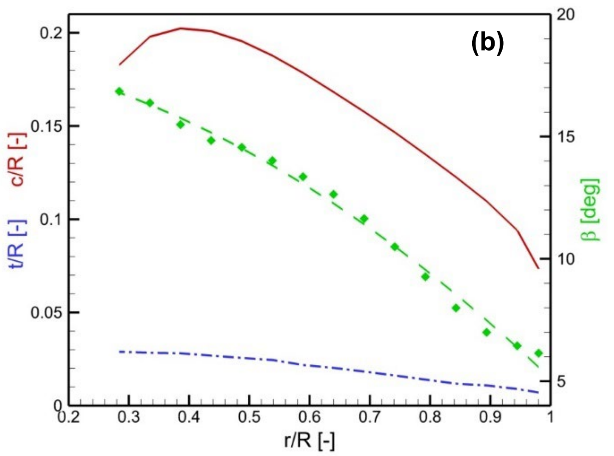

Figure 3. Blade isometric view and airfoil sections highlighted by colours (a); radial distribution of normalized chord c/R (red line), normalized thickness t/R (blue dash-dot line), and blade pitch β (green diamond marker) and second order interpolating polynomial (green dashed line) (b).

To measure the propeller aerodynamic loads, the Kubler encoders were removed and the motors were fixed to the ATI Mini 40 balance. Balance full-scale values and accuracy are indicated in Table 1. The measurements were carried out at a sampling frequency of 1000 Hz for a time of 20 seconds. Mean forces and moments were evaluated together with the standard deviation.

The rotor configuration, shown in Figure 4, resulted from the rotor rig setup. Only the loads on rotor 1 were measured, while the second rotor was placed on a dummy balance to maintain symmetry. Rotational speed was monitored by a single microphone placed near the propellers. The microphone used was a Gras model 40PK CCP, and data were collected at a sampling frequency of 12800 Hz for 30 seconds.

Table 1. Balance main specifications.

	F_x, F_y [N]	F_z [N]	M_x, M_y, M_z [Nm]
Full scale	±20	±60	±1
Accuracy (%FS)	0.25	0.60	0.0125

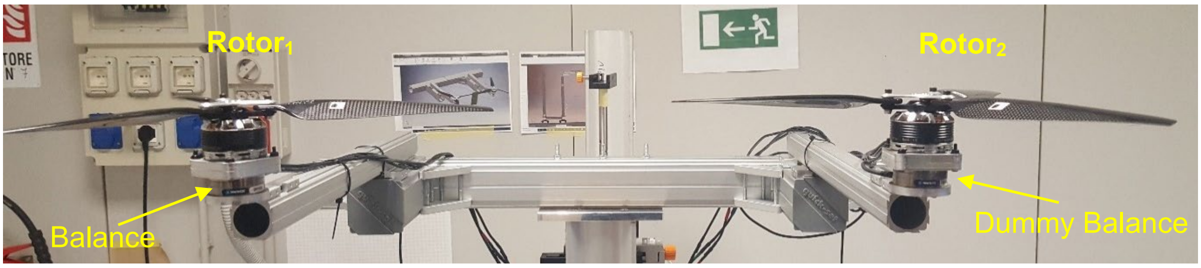

Figure 4. Rotor rig equipped with 6 components load cells

3.2 PIV measurement system

A two-component and stereo Particle Image Velocimetry (2C-PIV and S-PIV) measurement system measured the rotor downwash characteristics. The experimental configuration encompassed a dual-head Nd-Yag laser delivering a pulse energy of 180 mJ at a wavelength of 532 nm and operating at a repetition rate of 10 Hz. A recording system, composed of two ILA.PIV.sCMOS CLHS cameras, was employed. These cameras were mounted on a two-axis linear traversing system to enable an expanded measurement area through the horizontal displacement of the cameras. A single set-up was arranged for the various tandem configurations. The investigation of both the isolated propeller and the tandem configurations led to the installation of two cameras placed side by side and vertically aligned. This arrangement allowed for the observation of the wake evolution along the axial direction for more than one rotor diameter (Figure 5).

The measured region of interest for the isolated propeller covers the wake from x=0.23 R to x=1.17 R radially, and from z=0.1 R to z=-2.05 R vertically. For the tandem configuration, the recorded region is larger, ranging from x=0.5 R to x=1.75 R along the x-direction, and from z=0.09 R to z=-2.06 R vertically.

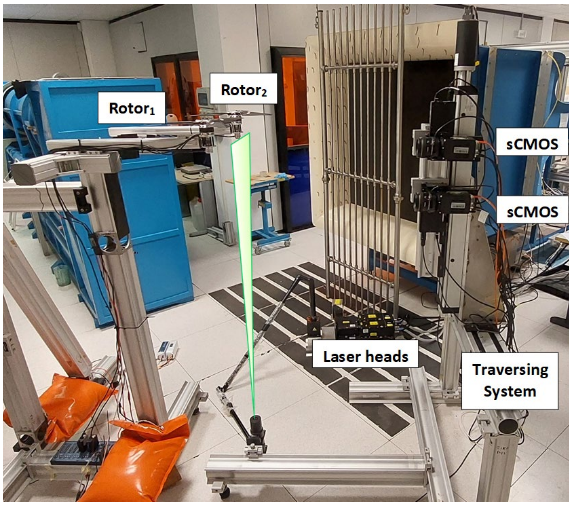

Figure 5: 2C-PIV layout: Tandem rotors

An overview of the measurement region for all configurations can be found in Figure 6.

As tracer particles, aerosolized diethylhexylsebacate (DEHS) oil was used. A seeding generator with 20 Laskin nozzles provided oil droplets with a size of less than 1 µm. The full test room was seeded to have a homogenous concentration of particles. The PIV images were pre-processed by applying a background grey-level subtraction. PivView v3.6.5 (by PivTech GmbH) was used to process the particle images. The particle images analysis consisted of an iterative multigrid cross–correlation algorithm ending at 32x32 px^2 and 50% overlap. The results presented a vector step of Δx=1.43 mm. The random noise of the PIV cross–correlation procedure can be estimated as 0.1 px as a rule-of–thumb (Raffel et al. in Ref. 18). Using the current values for the optical resolution (11.21 px/mm) and the laser double–pulse delay (45-60 µs), this is related to a velocity error of ε_u of ~ 0.2 m/s to 0.15 m/s.

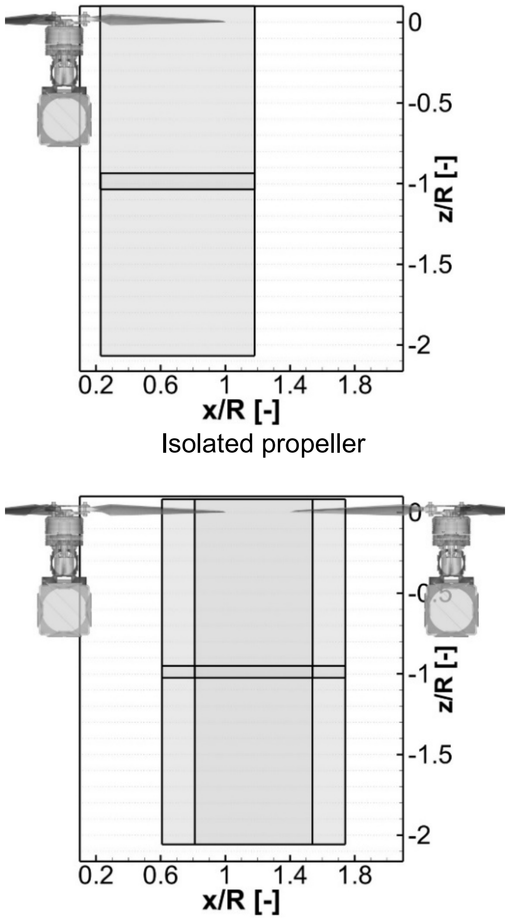

Figure 6: 2C PIV measurement regions

Three components flow field measurements (S-PIV) were carried out to investigate the isolated or multiple slipstream cross-flow at z=-0.51 R, the layout is depicted in Figure 7. A larger region was recorded at the expense of the spatial resolution. For the isolated and tandem at d=1.02 D configurations, the measured region covers radially the wake in the range between x=0.2 R to x=1.6 R and horizontally from y=-0.42 R to y=0.42 R. Increasing the interaxial rotor distance the radial boundary is shifted up to cover the region of x=0.4 R to x=1.9 R for the larger distance. The measurement areas are depicted in Figure 8. The S-PIV images have been processed using the same parameter of the two-component measurements and proving a vector step of $\Delta x = 2\,mm$. Due to the recording geometry and the measurement uncertainty, the out-of-plane measurement error ε_w can be assumed to be approximately a factor of √2 higher than that of the in-plane measurement, ε_w of ~ 0.28 m/s to 0.21 m/s. A preliminary description of the measurement setup and a discussion of the experimental results was given by De Gregorio et al. (Ref. 18).

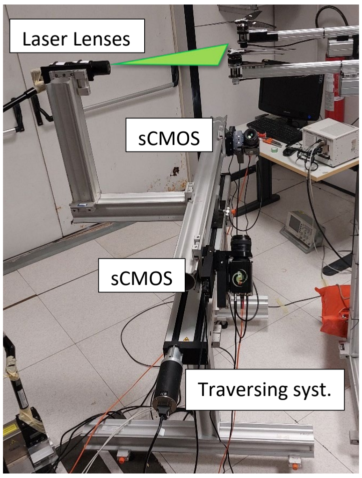

Figure 7: S-PIV layout, tandem configuration

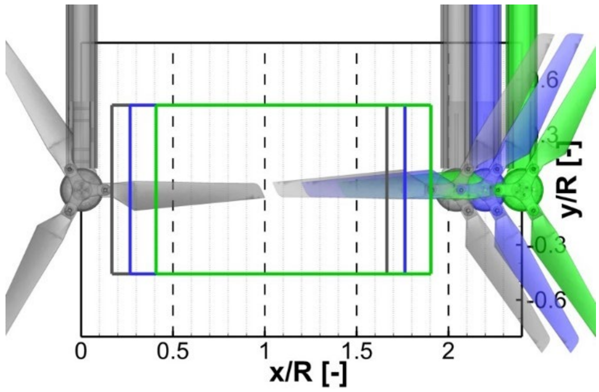

Figure 8: S-PIV measurement regions for the different tandem configurations: grey line for d = 1.02 D, blue line for d = 1.1 D and green line for d = 1.2 D.

3.3 *Acoustic measurement system*

The far-field acoustic measurements were performed within the CIRA semi-anechoic chamber. The propeller discs were vertically oriented and the rotating axes were placed at a height of 1.5 diameters from the ground. The rotor rig was placed in the centre of the semi-anechoic chamber with dimensions equal to 5.65(L) x 4.45(W) x 4(H) m^3 and characterized by a cut-off frequency of 90 Hz (Figure 9-a).

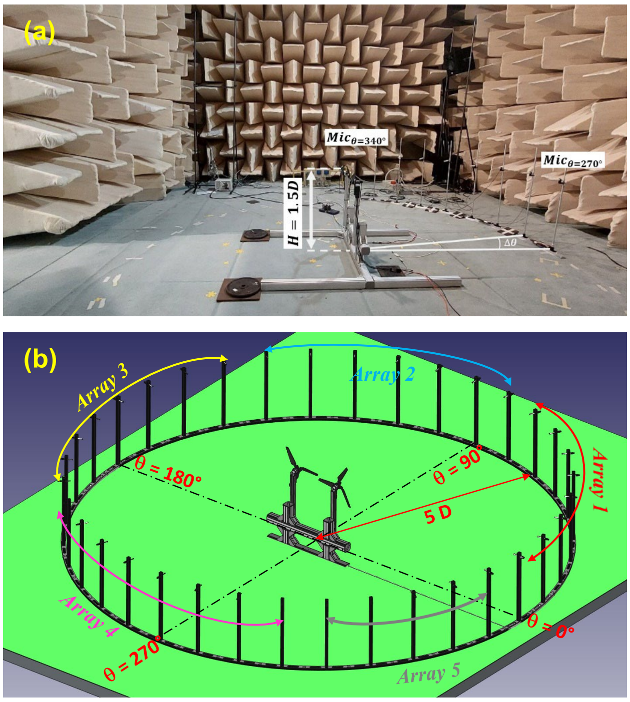

Figure 9: Rotor rig and microphone array: in the semi-anechoic chamber (a) and resulting layout (b)

An array of eight G.R.A.S. 40PK CCP microphones was positioned 5 meters away from the midpoint of the two rotors. The microphones were arranged in a semicircular modular structure with an angular spacing (Δθ) of 10 degrees, creating a total arc of 80 degrees. To cover the entire circumference around the rotors, the microphone array was moved along the azimuthal direction, covering a total of five positions. (Figure 9-b).

Each microphone had a frequency range of 20 to 20000 Hz and a dynamic range of 26 to 145 dB(A). An NI LabVIEW software was implemented to acquire pressure fluctuation data by using two NI 9234 modules of 4 channels each and NI cDAQ 9174 acquisition board. Data were acquired at a sampling frequency of 12800 Hz for 30 seconds. Finally, the pressure signals were filtered with a band-pass filter, over the frequency range from 90 Hz to 5.6 kHz.

4 RESULTS

4.1 Aerodynamic Results

The study examined the aerodynamic performance of isolated and tandem rotor configurations by varying the rotational speed. Figures 10 (a) and (b) show the mean values of thrust (Fz) and torque (Mz) for the isolated rotor, plotted against the rotational speed as red markers.

Both thrust and torque increase in absolute values as the rotational speed (Ω) increases, following a second-order polynomial law. The error bars in the chart represent the standard deviation of the data. When the rotors are arranged side by side, there is a decrease in thrust across the full velocity range and an increase in force fluctuation. This is evident from the higher thrust standard deviation compared to the single rotor configuration. The force fluctuation increases up to 20% of the average value, compared to 3% for the single rotor, which is in line with a previous study by Zhou et al. (Ref. 7). This study found a 2% decrease in thrust for twin rotors at a distance of d = 1.05 D, along with a significant increase in force fluctuation.

Chen et al. (Ref. 9) conducted experiments and observed that with a disk loading of 45 N/m^2 and the rotor distance at 1.025 times its diameter (D), there was a 5% reduction in thrust. They concluded that the loss of thrust was influenced by disk loading, and the higher the propeller loading, the greater the reduction in thrust. In the current study, the disk loading was 181 N/m^2 at a rotational speed of 5200 RPM, and a 6.3% reduction in thrust compared to the isolated rotor was recorded.

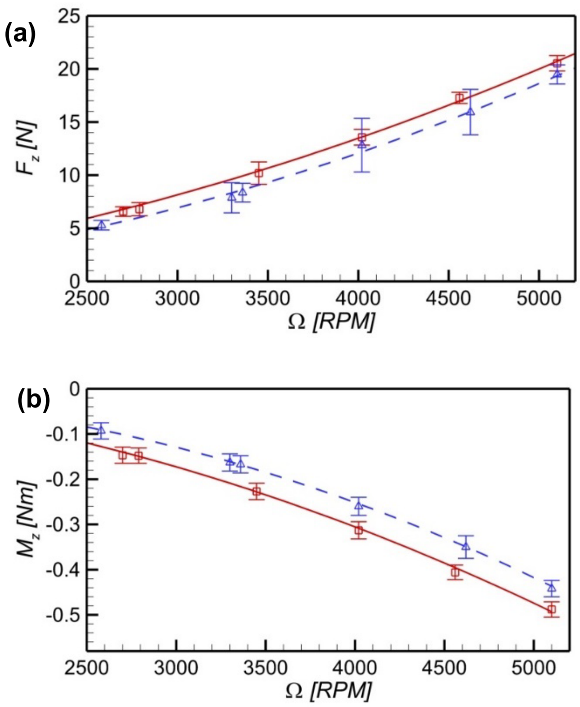

Figure 10: Thrust (a) and torque (b) of the isolated rotor (in red square markers) and tandem d=1.2 D (blue triangle). The 2nd-order polynomial fitting lines are plotted, a solid red line for the single propeller data and a dashed blue line for the tandem configuration. The error bars indicate the standard deviation of the present dataset.

The wake interaction has an impact on the rotor torque, leading to a decrease in absolute values across the entire speed range. The torque fluctuations exhibit similarities to the single propeller case. Consequently, when two rotors interact, there is a reduction in both thrust and torque, suggesting a corresponding decrease in blade drag.

4.2 Ensemble Average Velocity Fields

PIV measurements were conducted to examine the propeller slipstream characteristics for various rotor rig configurations. Ensemble average velocity fields were derived from a collection of five hundred instantaneous velocity fields obtained at different rotor azimuth angle positions.

The measured region of the isolated rotor (depicted in Figure 11-a) illustrates half of the slipstream. Through the vertical velocity colour map and streamtraces, an overview of the flow field behaviour is presented. The mean velocity demonstrates the typical wake contraction immediately downstream of the propeller disk, reaching a radial position of approximately x = 0.8 R at an axial distance of z = -0.5 R. In this contraction region, a positive gradient of the vertical velocity is observed, peaking at 18.2 m/s at z = -0.5 R and maintaining a nearly constant behaviour down to z = -1.25 R, as shown in Figure 11-b.

Moving further downstream, the peak velocity decreases to about 16.6 m/s at z = -2.0 R due to dissipative phenomena. The diagram indicates that the vertical velocity peaks from z = -0.5 R to z = -1.25 R are essentially equivalent, while the velocity slopes in the shear layer region decrease moving downward, consistent with flow diffusion.

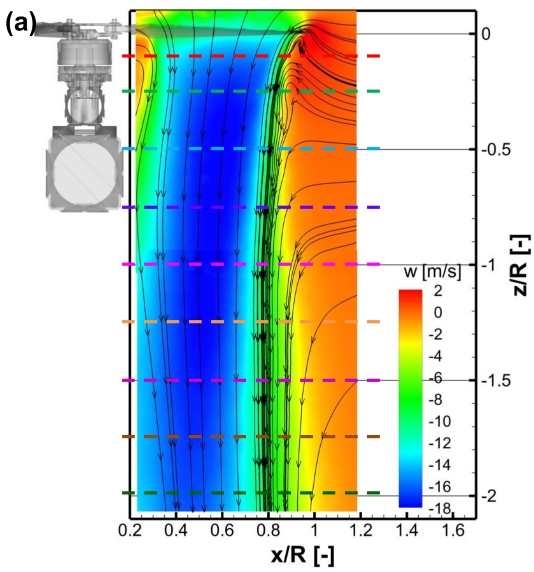

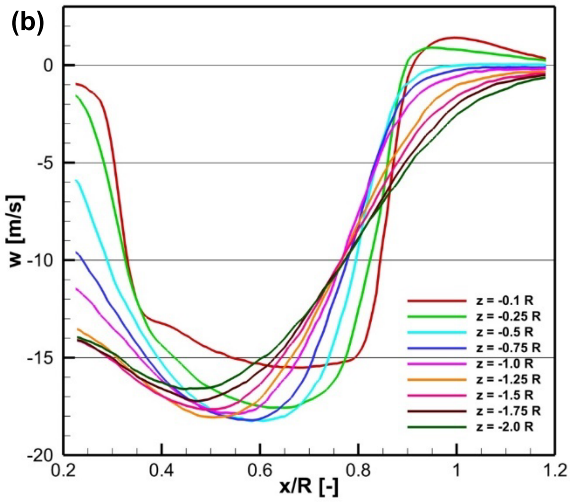

Figure 11: Iso-contours with streamtraces of the ensemble-average flow field colour-coded with the velocity vertical component at Ω = 5200 RPM for isolated rotor (a) and extracted vertical velocity trend along radial distance for different z-stations (b)

The mass flow entrainment from the external undisturbed region is described by the streamlines. In the region between the propeller disc and the plane z = -0.4 R, an upstream flow direction is evident due to the shedding of the tip vortices. Downstream, the streamtracers bend downward as they enter the propeller slipstream, a behaviour confirmed by the axial velocity curves at z = -0.1 R and -0.25 R, exhibiting clear upwash in the outer flow region between 0.9 R < x < 1.2 R.

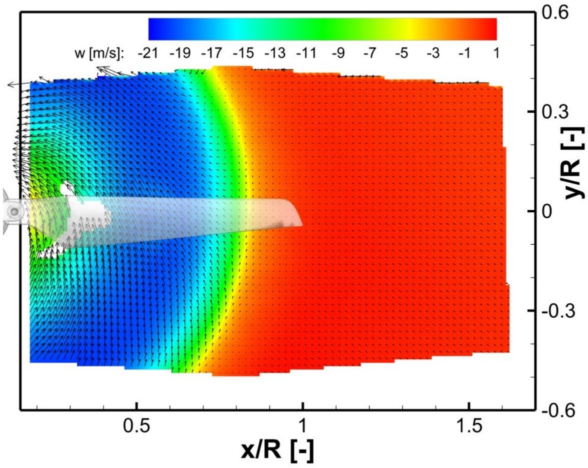

Figure 12: Three-component mean velocity field at z = -0.51 R. The in-plane velocity components are depicted by black arrows while the axial flow component is colour-coded

The three-components average velocity field on the xy plane at z = -0.51 R is depicted in Figure 12. The slipstream appears nearly circular, with the shear layer and maximum induced velocity shown in green and blue colours, respectively. At z = -0.51 R, the inner region of the wake shows a radial slipstream contraction of about x = 0.75 R, which aligns with the findings in Figure 11-b.

In this study, the wake interaction for Tandem configuration was thoroughly investigated through the acquisition of 500 instantaneous velocity fields for each case. The velocity fields were obtained with propellers in a free state or with a controlled blade phase. The mean velocity fields of the tandem configurations at different inter-axis distances (d = 1.02 D, d = 1.1 D, and d = 1.2 D) for a co-rotating speed of Ω = 5200 RPM are illustrated in Figure 13.

The observed velocity field demonstrates a noticeable slipstream deviation attributed to the interference of the rotor with respect to the isolated rotor behaviour. Moreover, the streamlines depict a mutual attraction between the rotor slipstreams, with the wake deviation becoming more pronounced as the rotors are positioned closer together. Additionally, the streamlines indicate a preferred direction toward the slave rotor, showcasing a non-symmetrical wake behaviour.

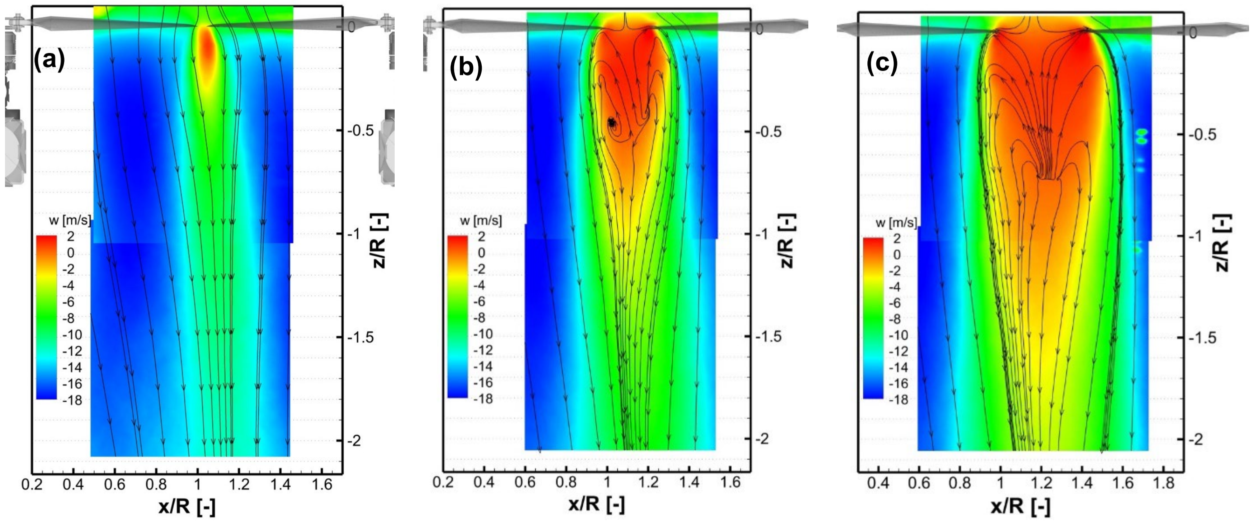

Figure 13: Co-rotating side-by-side rotor vertical velocity colour map for different interaxial distances d = 1.02 D (a), d = 1.1 D (b) and d = 1.2 D (c)

An improved understanding of the tandem co-rotating configurations can be gained by comparing the axial velocity component for different configurations at varying distances from the rotor disk (Figure 14).

At the closest tandem distance (d = 1.02D) just downstream of the rotor disk, at z = -0.1 R (Figure 14-a), the induced axial velocity between the slipstreams is almost negligible due to intense flow interaction, eliminating the blade tip vortex upwash. The steep slopes indicate the slipstream shear layers, reaching the inner regions with maximum axial velocities. The peak velocity of the slave slipstream is smaller than that of the main rotor, indicating asymmetry.

Different observations can be made for the tandem cases with larger distances. In the middle region between rotors, the induced axial velocity shows an upwash due to the released blade tip vortices, with small slopes indicating a slight shear layer and notable acceleration leading to axial velocities similar to those in the tandem configuration with d = 1.02 D.

Moving away from the disk at z = -0.5R (Figure 14-b) for the closest tandem configuration, the axial velocity accelerates to w = -7 m/s in the region between the two slipstreams, indicating that the slipstreams have already joined.

The slopes of the shear layer decrease due to significant flow diffusion. The inner slipstream velocity increases similarly to the isolated rotor's velocity. The velocity slope is shifted toward the slave rotor.

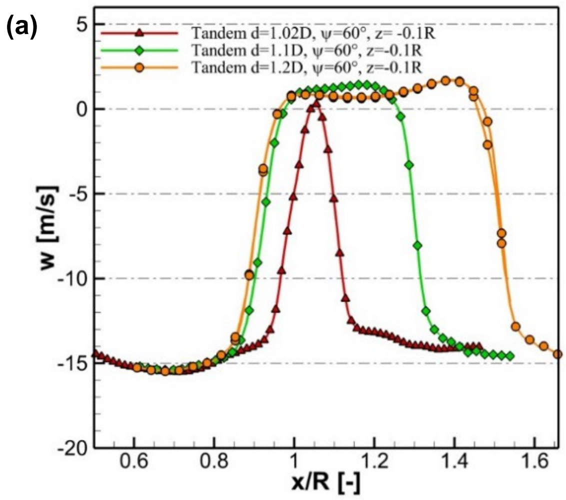

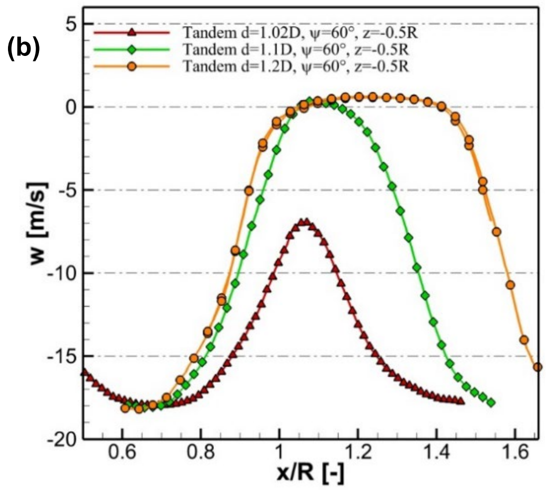

Figure 14: Axial velocity comparison for co-rotating tandem configurations at z = -0.1 R (a) and z = -0.5 R (b).

For the tandem configuration with d=1.2D, the axial velocity between the rotors is almost zero or has a slight upwash, and the shear layer slopes show a less pronounced behaviour, suggesting the occurrence of flow diffusion. Eventually, the maximum speed inside the wake is reached, equal to the tandem configuration with the smallest distance. Similarly, when moving downward, the velocity envelope is deflected toward the slave rotor.

A quantitative analysis of the wake deviation is conducted by comparing the induced vertical velocity at varying distances from the rotor disk. To keep it concise, only the axial velocity comparisons at a distance of z = -0.1 R and z = -0.25 R are shown in Figure 15.

The deviation of the slipstream from the isolated case is measured as a percentage displacement for the three tandem configurations. In the tandem configuration, the main rotor slipstream moves towards the slave rotor.

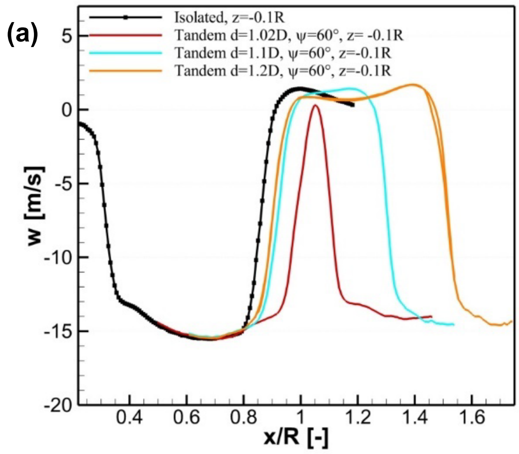

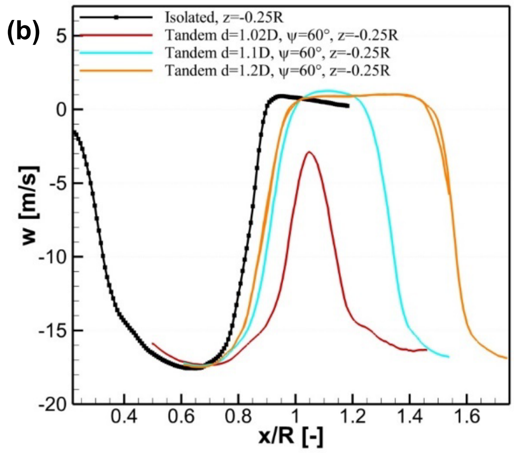

Figure 15: Isolated and tandem rotor configurations comparison of axial velocity at a distance of z = -0.1 R (a) and z = -0.25 R (b) from the rotor disk

The displacement at z = -0.1 R is approximately 15% for the closest distance and reduces to 5% for an interaxial distance of d = 1.2D, while at z = -0.25 R, it is translated to larger values. The slipstream distortion demonstrates a second-order polynomial behaviour in relation to the rotor distance normalized with respect to the propeller radius, as illustrated in Figure 16.

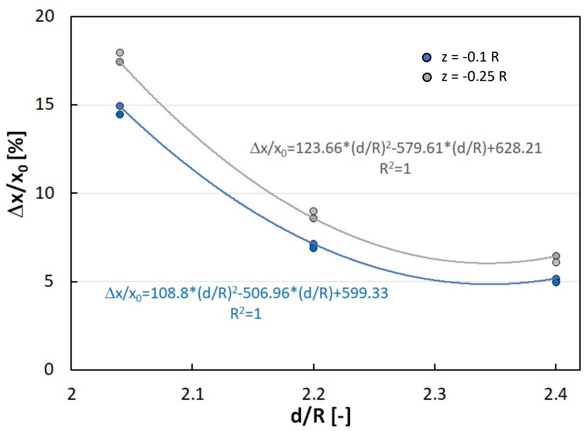

Figure 16: Slipstream deflection versus the normalised rotor interaxial distance

The average velocity fields of the tandem configurations at different interaxial distances of d=1.02D, d=1.1D, and d=1.2D for a counter-rotating speed of Ω = 5200 RPM are shown in Figure 17. Similar to the co-rotating configuration, the axial velocity contours are calculated based on 500 instantaneous velocity maps, providing information about the averaged flow acceleration inside the propeller wake and the location of the shear layer. The velocity maps show a deviation in the slipstream due to interactional effects as compared to the isolated rotor. In contrast to the co-rotating cases, the streamlines highlight two large counter-rotating circulation zones near the blade tips, leading to an increase in upwash between the two rotors. The counter-rotating cases exhibit symmetric behaviour, with both rotors reaching the same peak velocity values.

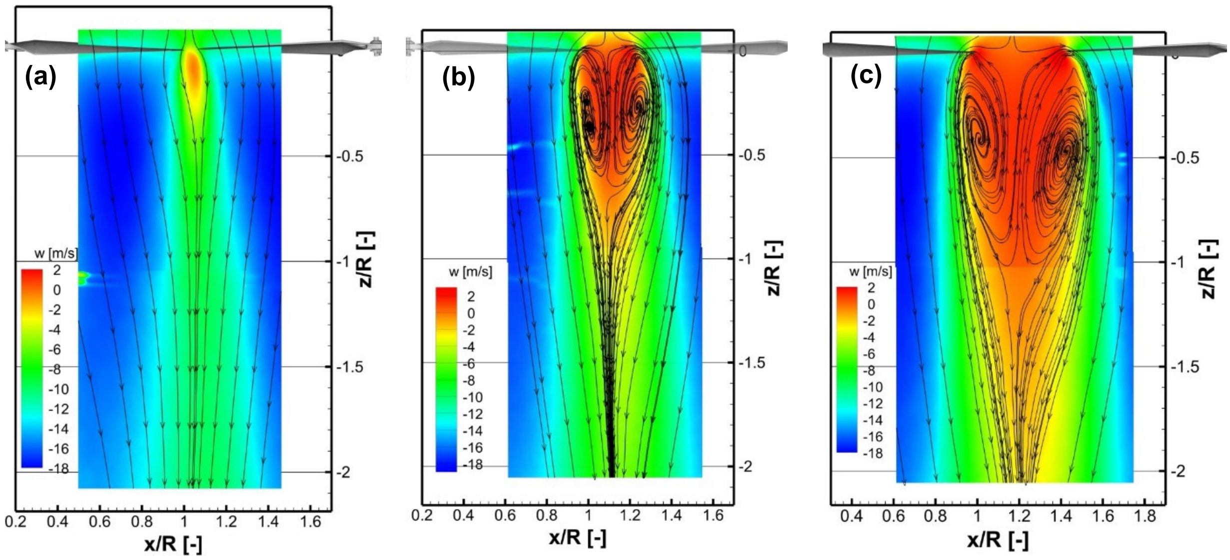

Figure 17. Counter-rotating side-by-side rotors vertical velocity colour map for different interaxial distances d=1.02D (a), d=1.1D (b) and d=1.2D (c)

A quantitative comparison between the co-rotating and counter-rotating twin cases of the axial velocity is depicted in Figure 18.

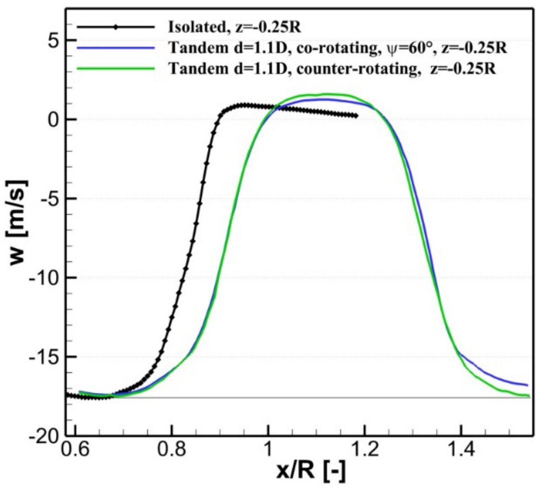

Figure 18: Isolated and co/counter-rotating twin rotor at a distance of d=1.1D configurations comparison of axial velocity at a distance of z = -0.25 R from the rotor disk.

In the case of counter-rotating propellers, the results show that there is symmetrical behaviour, with the same velocity values within the slipstream. Additionally, there is a slightly higher upwash in the region between the two propellers. It's important to note that the deviation of the shear layer is not affected by the direction of rotation. When the main rotor is in a tandem configuration, the displacement of the slipstream depends only on the relative distance and is not affected by the direction of rotation.

The stereo PIV measurements carried out on the axial orthogonal plane at a distance of z = -0.51 R shed light on the behaviour of the flow field for co-rotating and counter-rotating tandem configurations (Figure 19).

It's worth noting that while the airflow behind a single rotor formed a circular distribution, the dual-rotor configuration resulted in a droplet-shaped velocity field due to the flow disturbance from the neighbouring rotor. This observation aligns with the findings of Zhou et al. (Ref. 7) on a counter-rotating twin-rotor and Lee et al. (Ref. 10) on a quadcopter. In the case of counter-rotating rotors, the airflow displays two opposing protuberances, as illustrated in Figure 19 b, d and f. The vector plots present a symmetric behaviour of the slipstreams and an inward side wash for all the interaxial distances as indicated by the black arrow in Figure 19. The co-rotating tandem configuration presents a different flow behaviour. While the main rotor slipstream deformation is similar in terms of shape and location to the counter-rotating cases the slave rotor slipstream protuberance is located in the opposite direction of the x-axis, i.e. instead of left up it is on left down of the image. The flow region between the two rotors has a clockwise recirculation zone.

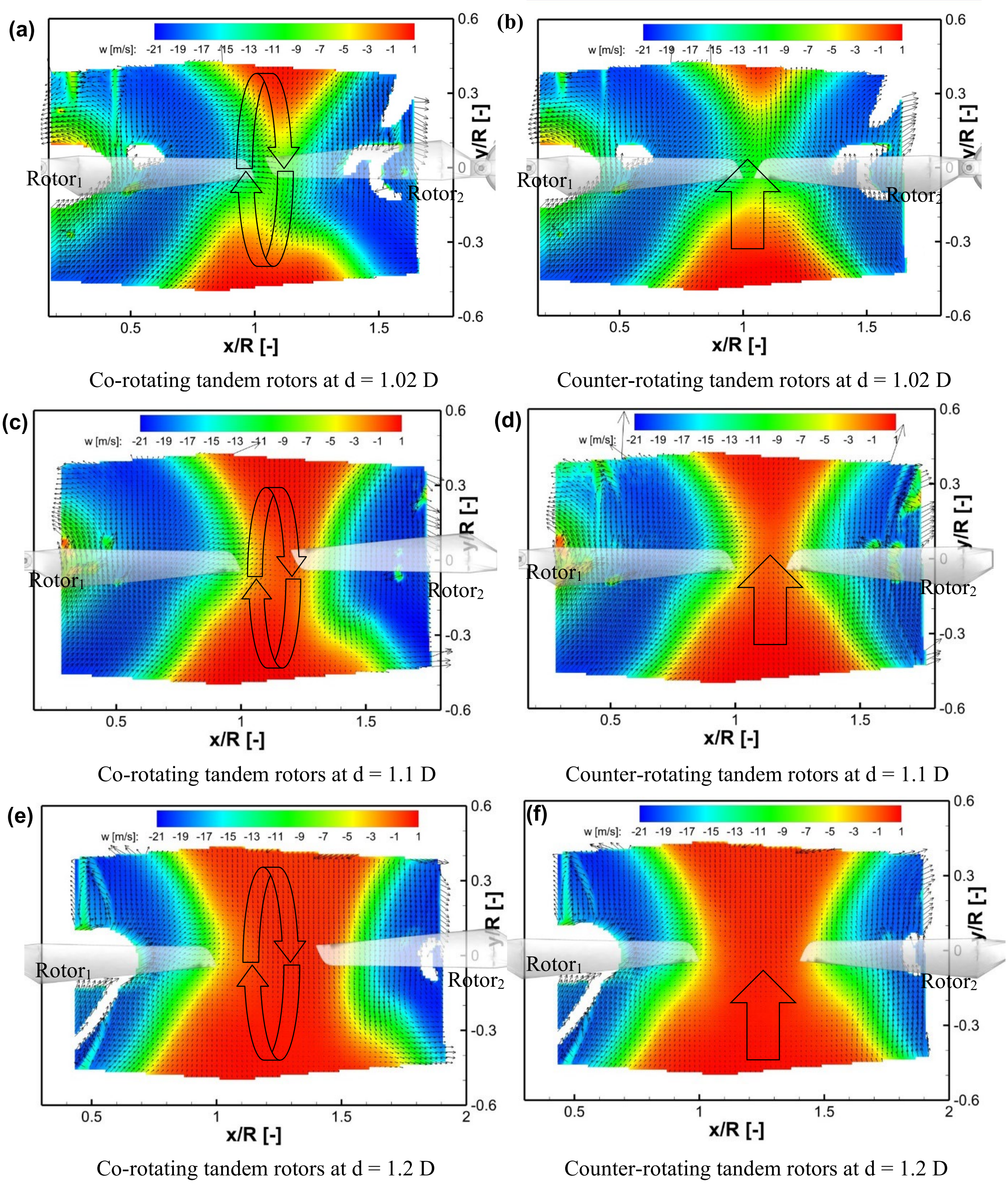

Figure 19. Three-component mean velocity field at z = -0.51 R for co-rotating (a, c, e) and counter-rotating (b, d, f) configurations. The in-plane velocity components are depicted by black arrows while the axial flow component is colour-coded.

Quantitative results regarding the deformation of wake geometry are presented in Figure 20 to Figure 22.

The iso-velocity line, derived from the mean velocity fields for different configurations, effectively represents the shapes of the slipstreams. Figure 20 illustrates the wake geometry for both the isolated rotor and the main rotor in tandem configuration across various cases. As previously mentioned, the wake geometry of the isolated rotor appears nearly circular (black line). In contrast, when in tandem configurations, the slipstream initially follows a circular path up to an azimuthal angle of $\theta = -15°$, then diverges, creating protuberances directed towards the secondary rotor.

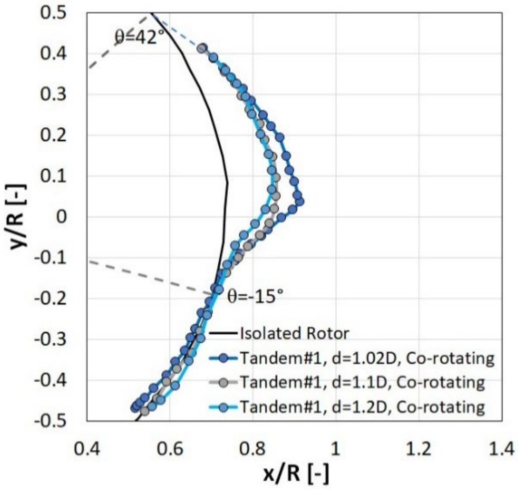

Figure 20: Axial velocity isolines (w=-16.5m/s) at z=-0.51R for isolated and tandem cases varying the interaxial distance

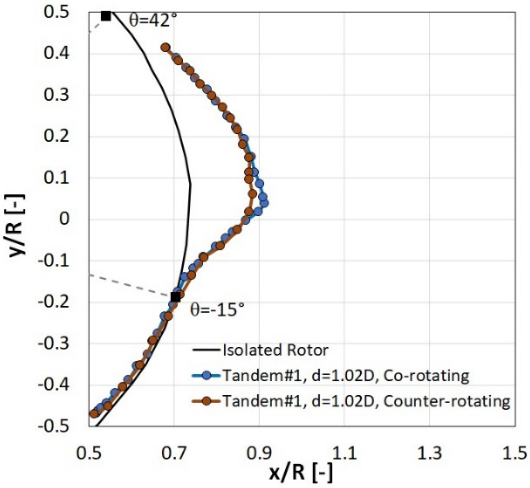

Figure 21: Axial velocity isolines (w=-16.5m/s) at z=-0.51R for isolated and twin rotors with d=1.02D for co-rotating and counter-rotating cases

The deformation of the slipstream geometry is inversely related to the distance between the rotors. At an azimuth angle of $\theta = 42°$, the results suggest that the slipstream resumes a circumferential shape.

In Figure 21 the geometry of the main rotor slipstream for tandem configurations with a distance of d=1.02D is compared for co-rotating and contra-rotating velocity. The results indicate the same geometry for both cases, which confirms the findings obtained from the axial velocity components (Figure 18).

In Figure 22, the slipstream geometries for all the cases under investigation are summarized. The geometries of the secondary propeller are visible. In the co-rotating slipstream cases, the peak of the protuberances is directed in the azimuthal range between 185 and 195 degrees. Conversely, in the contra-rotating cases, the protuberance peak is oriented between 165 and 175 degrees.

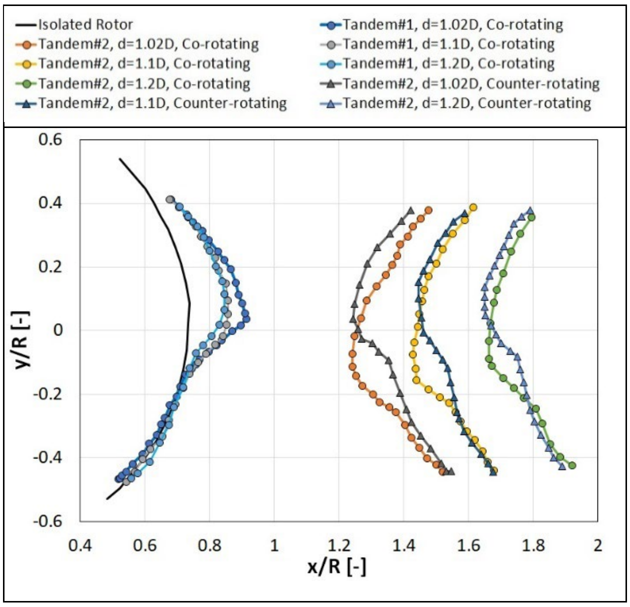

Figure 22: Rotor slipstream geometry for co-rotating and counter-rotating cases

4.3 Acoustic Results

In this section, the results of the acoustic investigation are reported. For the sake of brevity, only the results corresponding to the mutual distance $d/D = 1.02$ are reported, and these are compared with those corresponding to the isolated rotor, to assess the phase effect on noise impact. The results are reported in terms of OverAll Sound Pressure level (OASPL) in the form of a directivity diagram. The OASPL is defined as:

$$OASPL = 10\ \log_{10}\left(\frac{\sigma}{p_0}\right)^2$$

where the σ is the standard deviation of the pressure time series evaluated as:

$$\sigma = \int_{f_1}^{f_2} PSD(f)df$$

being f_1 and f_2 the extremes of the region of interest, in the present case set to cover the entire microphone linear operating range, and the PSD is the Power Spectral Density of the pressure signal expressed in Pa^2/Hz. Moreover, p_0, equal to $20\ \mu Pa$, is the minimum audible pressure for the human ear and is used as a reference value.

The polar diagrams are reported in Figure 23. The main evidence is that the isolated propeller exhibits monopole-like behaviour, as expected by the literature, (Ref. 10), whereas the tandem configuration tends to have dipole-like behaviour. As a result, most of the effects are addressed to the rotor disk region. Specifically, for $\theta = 0°$ and $\theta = 180°$, the tandem configuration shows a noise reduction of approximately 6-7 dB. This phenomenon is associated with a significant increase in noise in the inflow region. Furthermore, regarding the tandem configuration, a very complex behaviour was observed, and it is not possible to identify a clear trend. It should be noted that the polar diagram is asymmetric with respect to the rotor axis; this effect is attributable to the blade rotation direction. Interestingly, among the tandem configurations, the one associated with the least acoustic impact in the rotor disk region is the same as the one associated with the greatest acoustic impact in other regions, characterized by a phase delay of $\psi = 60°$.

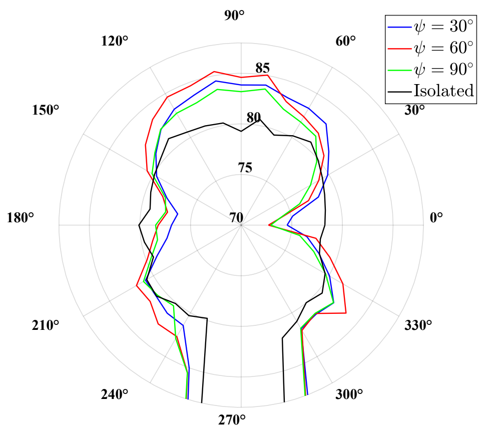

Figure 23: OASPL (dB), twin propellers at $d/D = 1.02$ for different phase angles compared to the isolated propeller.

Since the greatest acoustic effect is concentrated in the rotor plane for the two characteristic polar angles, a spectral analysis was performed, and the results are presented in Figure 24.

The results are reported in the dimensionless form of the Sound Pressure Spectrum Level (SPSL), that according to Ref. 20, is defined as:

$$SPSL = 10 \log_{10}\left(\frac{PSD\ \Delta f}{p_0^2}\right)$$

where Δf is the frequency resolution set equal to 1.

The differences observed in the tonal peaks are due to small variations in the rotational speed, primarily related to the stability of the control system but quantifiable within a margin of less than 5% compared to the reference value.

The most significant finding is that when transitioning from the isolated configuration to the tandem configuration, the main noise component changes. In the first case, the pressure field is dominated by the broadband component, whereas in the tandem case, there is a substantial increase in the energy associated with the tonal component.

Additionally, it is observed that for $\theta = 0°$, the noise associated with the first and second harmonics is more intense in the isolated configuration compared to the tandem configuration. Conversely, the subharmonics are more intense in the tandem configuration. This occurs because, in the case of the isolated rotor, the subharmonics are buried in the broadband component. This behaviour does not occur for $\theta = 180°$; in this case, the primary harmonic is associated with a phase delay of 90° , while for $\psi = 30°$ and $\psi = 60°$, the acoustic impact is essentially the same.

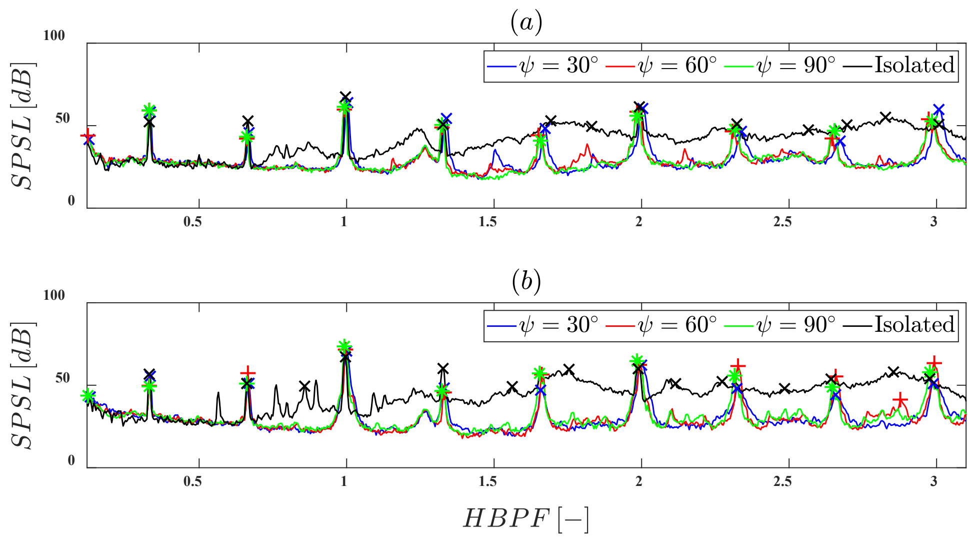

Figure 24: Dimensionless spectra of the pressure signals at fixed distance $d/D = 1.02$ at $\theta = 0°$(a) and $\theta = 180°$(b) for different values of the propeller phase delay compared to the isolated propeller.

To better understand the effect of phase delay on the tonal component, the Band-Limited Sound Pressure Level (BLSPL) for the first and second harmonics was calculated and the results are presented in Figure 25. The analysis of individual harmonics reveals a strong directivity of the noise source. This is highlighted by the pronounced asymmetry of the diagram corresponding to the first harmonic (Figure 25 a), particularly in the $\theta = 180°$ region, which shows a much higher acoustic impact compared to $\theta = 0°$. The behaviour of the second harmonic (Figure 25 b) is especially interesting for a phase delay of $60°$, where a dipole-like pattern is observed in the polar diagram, while the other two tandem configurations behave like a monopole. In addition to the different shapes of the polar diagram, the curve for $\psi = 60°$ also shows the highest intensity, except for the $\theta = 180°$ angle, where it exhibits the minimum BLSPL value.

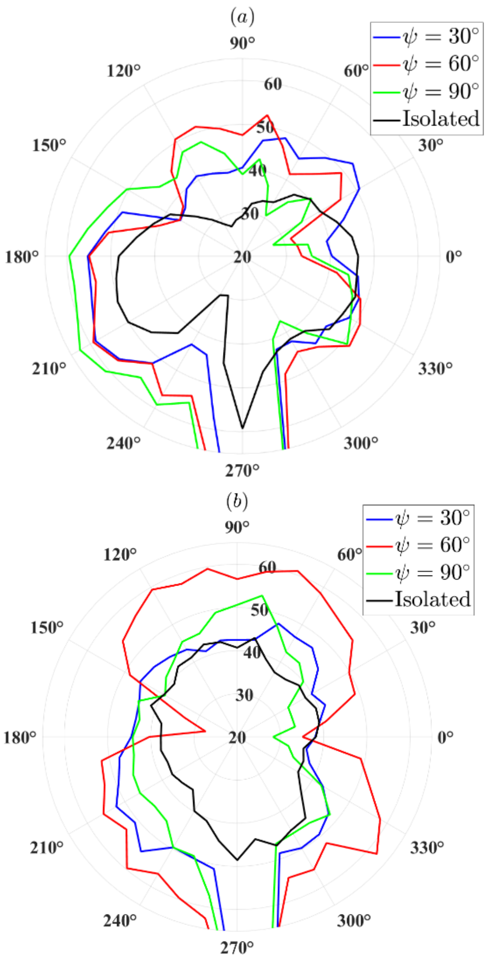

Figure 25: BLSPS (dB), twin propellers at $d/D = 1.02$ for the first (a) and the second (b) Harmonics for different phase shifts compared to the isolated propeller.

As a result, an acoustic effect can be achieved and it is highly dependent on the polar angle. This implies that it is possible to optimize the tonal noise component, which is the most annoying for humans, in certain spatial regions while accepting constructive interference (and a consequent increase in noise) in other spatial regions.

Additionally, to investigate the acoustic differences between the corotating and contra-rotating configurations, the results from the corotating case at $\psi = 30°$ were compared with those associated with the counter-rotating configuration. The configuration $\psi = 30°$ was chosen as it exhibits the minimum OASPL value in the polar diagram.

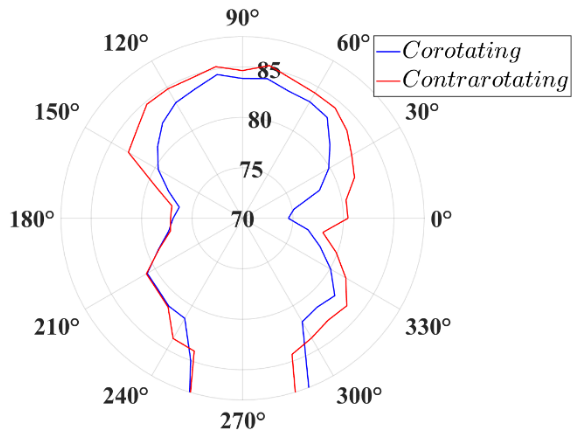

Figure 26: OASPL (dB), twin propellers at $d/D = 1.02$ for co-rotating and contra-rotating configurations

As in the previous case, to obtain an ensemble measure of the acoustic impact, the OASPL was calculated in the form of a directivity diagram (Figure 26). The main result is that the counter-rotating configuration is characterised by a higher acoustic impact for every polar angle, except in the region between 180 and 240 degrees where the values overlap. The noise increase is quantifiable at 3-4 dB.

Moreover, the spectral analysis sheds light on the different behaviours between the two configurations and helps to understand the reasons for the differences in acoustic impact. What is observed in Figure 27 is that in the contra-rotating configuration, there is a significant increase in the broadband component compared to the co-rotating configuration. This can be physically interpreted as the different direction of rotation results in constructive interference and an increase in the turbulence in the rotor region leading to an increase in the broadband noise component.

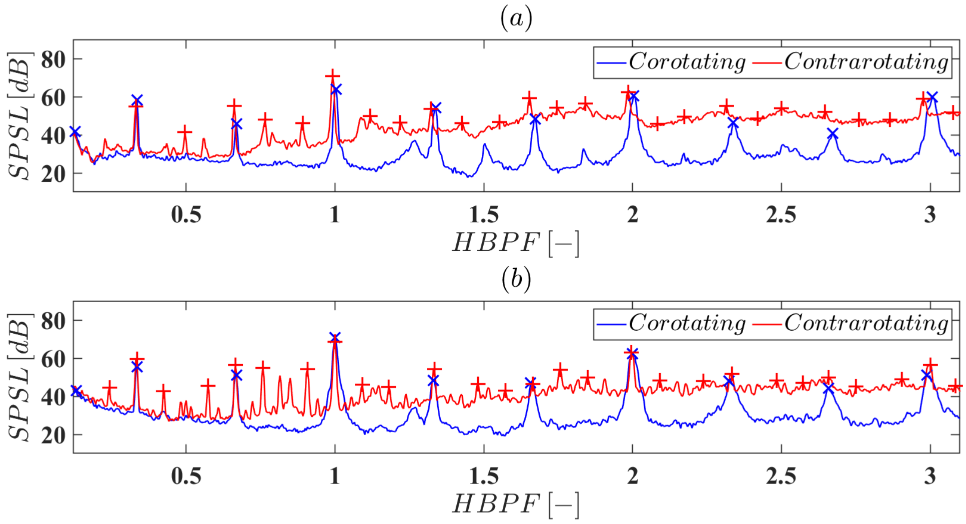

Figure 27: Dimensionless spectra of the far-field pressure signals for the co-rotating and the contra-rotating configurations at fixed distance $d/D = 1.02$ at $\theta = 0°$(a) and $\theta = 180°$(b).

Finally, having observed that in the rotor plane the tonal noise is almost the same between the two configurations, the BLSPL for the first two harmonics was calculated, and the results are reported in the Figure 28. The most relevant result is that the first harmonic for the counter-rotating propellers has a higher acoustic impact compared to the co-rotating configuration, with peaks exceeding 15 dB. Regarding the second harmonic, it is observed that in the rotor plane, the two configurations have comparable acoustic impacts, while in the inflow region, the counter-rotating configuration shows a noise increase of about 10 dB.

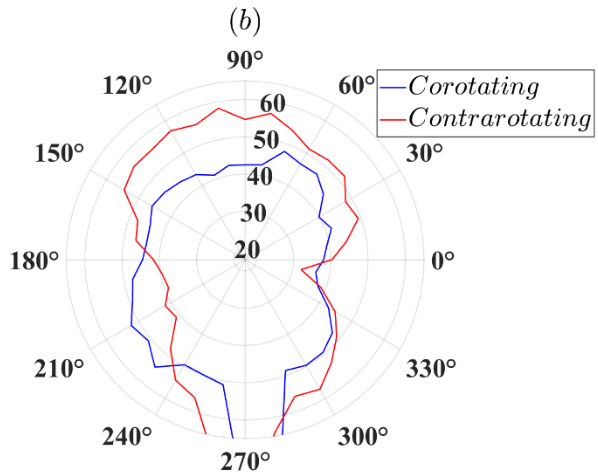

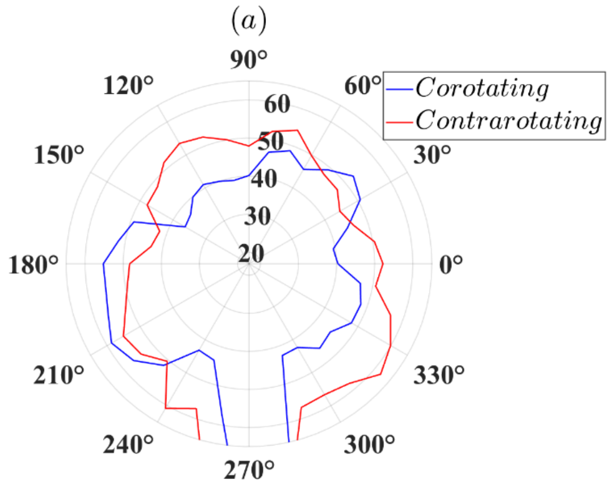

Figure 28: BLSPL (dB) for co-rotating and contra-rotating configurations at $d/D = 1.02$ for the first (a) and the second (b) harmonics.

Moreover, to assess how interference effects are modified by the distance between the propellers, an analysis was conducted at a fixed phase angle while varying the spacing between the rotors. Figure 29 reports the results in terms of OASPL. As expected, at the minimum distance of d/D=1.02, characterised by maximum interaction, the noise is higher along the entire polar domain. It is interesting to note that for the two distances d/D=1.1 and d/D=1.2, the acoustic impact is essentially the same, with a slight decrease associated with the greater distance in the arc between 30 and 70 degrees. This behaviour suggests that as the distance increases, the system moves out of the interaction zone, and the effects tend to become negligible. This phenomenon, which requires further investigation, would allow us to associate an interaction noise value of approximately 2 dB at the minimum distance. Additionally, we can attribute most of the interaction effects to the inflow region. However, a narrowing of the polar diagram in the rotor disk region is still observed due to the tandem configuration, suggesting that interaction effects are present at all distances but become less significant in the inflow region as the propellers are spaced further apart. The results of the spectral analysis are shown in Figure 30, focusing again on the rotor plane characterised by the lowest OASPL value. It is observed that for θ=0°, there are no significant differences with varying distances. In this region, pressure waves tend to sum up without being affected by the distance

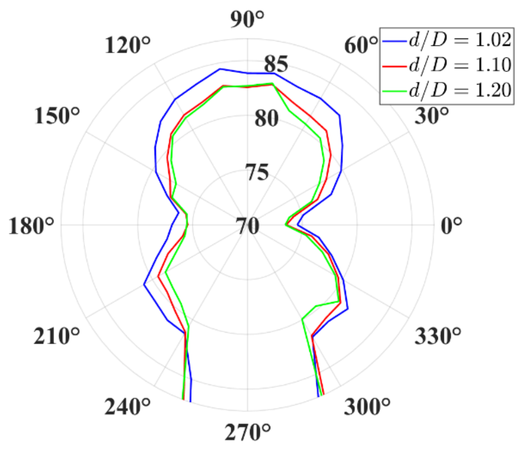

Figure 29: OASPL (dB), twin propeller at ψ = 30° for different interaxial distances.

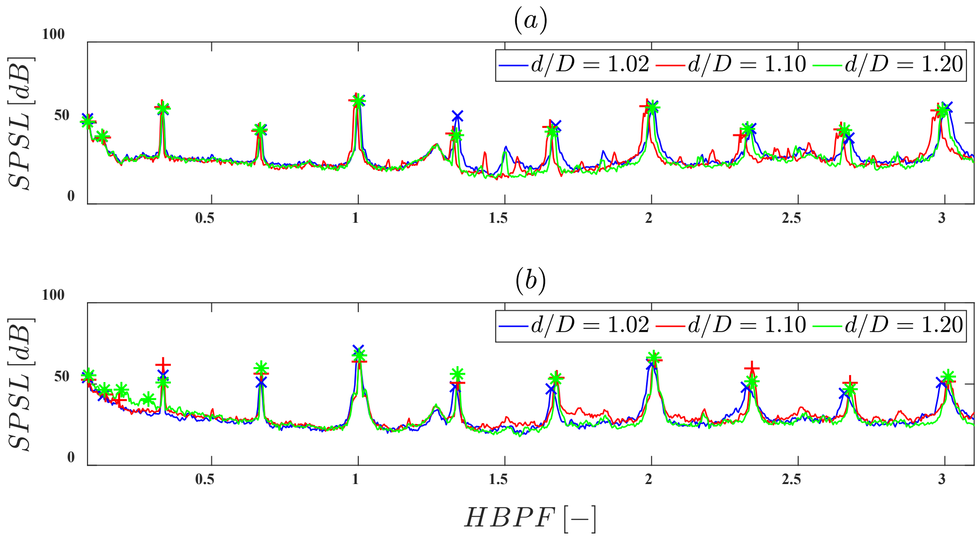

Figure 30: Dimensionless spectra of the far-field pressure signals at constant phase delay ψ = 30° at θ = 0°(a) and θ = 180°(b) for different rotor-to-rotor distances.

However, at θ=180°, there is a higher intensity of the first harmonic for the minimum distance, which becomes the lowest for the other harmonics and subharmonics. Increasing the distance between the propellers results in a shift of energy from the first harmonic towards the higher harmonics.

The results regarding BLSPL, as shown in Figure 31, confirm the overall findings. The highest noise for the first harmonic is linked to the shortest distance, especially in the area between 160 and 230 degrees. On the other hand, the two configurations with greater distances show very similar patterns. The behaviour of the second harmonic remains mostly consistent across different distances, indicating that interaction noise is mainly caused by the first harmonic, while its effect on higher harmonics is minimal.

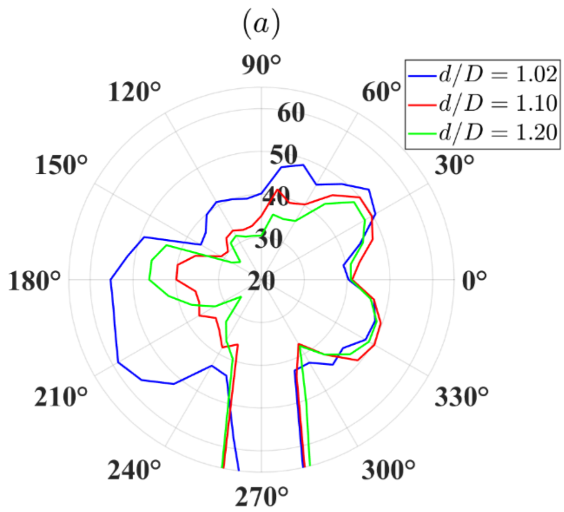

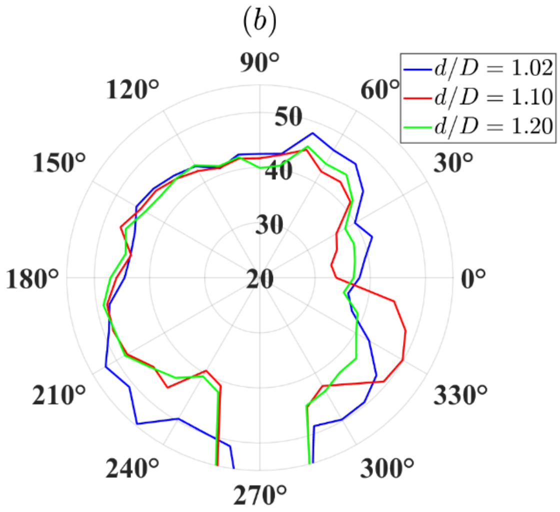

Figure 31: BLSPL (dB), twin propellers at phase angle of $\psi = 30°$ for the first (a) and the second (b) harmonics for different interaxial distances.

5 CONCLUSIONS

Extensive experimental investigations have been conducted to study the aerodynamic, fluid dynamic, and acoustic properties of three-bladed rotors in both isolated and side-by-side configurations during hover conditions. The research focused on examining the effects of slipstream interaction by varying the distance between the rotor axes and their rotation.

The aerodynamic performance of the propellers was evaluated across a range of rotational speeds spanning from 2500 to 5200 RPM. Concurrently, flow and acoustic measurements were specifically taken at a consistent rotational speed of 5200 RPM.

It was observed that as the rotor axes approached each other, there was a noteworthy decline in aerodynamic performance, with the most pronounced effect occurring at the closest configuration, denoted as d=1.02D. This resulted in a reduction in thrust by a range of 6% to 15%, and torque by 12% to 26%, in comparison to the baseline measurements obtained when the rotor was considered in isolation.

The side-by-side rotor configuration introduces interaction between slipstreams, leading to alterations in their flow patterns. Velocity maps have been instrumental in elucidating these deviations, which demonstrate an attractive effect between the slipstreams as they deviate from the main direction observed in isolated cases. This deviation follows a second-order law and becomes more pronounced as the axial distance between the rotors decreases. Additionally, while the verse of the rotation does not significantly impact the first rotor, it does affect the flow pattern of the second propeller.

The investigation reveals that in cases where rotors are co-rotating, there is a notable deviation of the slipstreams towards each other when observed along the radial plane. This deviation is less pronounced in counter-rotating cases. The analysis of induced tangential and radial velocities measured in cross-planes provides an explanation for this phenomenon. Downstream of the rotor disk, the wake loses its intrinsic circular symmetry, which is typical of an isolated rotor, and is instead replaced by a droplet-shaped footprint characterized by a lobe directed towards the near rotor wake. In co-rotating cases, the slipstreams display an asymmetric pattern with an undisturbed region deviated towards the near rotor wake, while counter-rotating cases exhibit a symmetric pattern of the lobes.

Additionally, the directivity pattern of the noise generated by the rotors placed side-by-side indicates an increase in intensity compared to that emitted by an isolated rotor. However, within the range of angles 0° ≤ θ ≤ 30°, 150° ≤ θ ≤ 190°, and 340° ≤ θ ≤ 360°, a reduction in noise emission has been observed, suggesting that the interaction of the slipstream contributes to noise mitigation. Furthermore, the distance between the rotor axes directly influences the noise emissions. Acoustic results demonstrate an increase in noise for the closest distance, i.e., d=1.02D, while no remarkable features are observed for distances of d=1.1D and 1.2D.

Similarly, the orientation of the blades impacts the amount of noise produced. Counter-rotating rotors generate both tonal and broadband noise, whereas co-rotating configurations produce less noise. This is because the flow interaction is greater in counter-rotating setups due to their symmetrical cross-flow geometry, compared to the asymmetrical geometry of co-rotating setups.

Author contact:

Fabrizio De Gregorio, f.degregorio@cira.it

Paolo Candeloro, paolo.candeloro@unicusano.it

Fabio Del Duchetto, fabio.delduchetto@unicusano.it

Tiziano Pagliaroli, tiziano.pagliaroli@unicusano.it

6 ACKNOWLEDGMENTS

The authors would like to thank their colleagues V. Quaranta, A. Sorrentino and G. Diodati for their availability during the measurements in the semi-anechoic chamber of the CIRA and G. Ceglia for his contribution during the PIV measurements.

The investigations described in the present paper were all carried out by the authors in the framework of the GARTEUR Action Group 26: “Noise Radiation and Propagation for Multirotor System Configurations”.

7 REFERENCES

1. Straubinger, A., Rothfeld, R., Shamiyeh, M., Büchter, K.-D., Kaiser, J., and Plötner, K. O., "An overview of current research and developments in urban air mobility–Setting the scene for UAM introduction," Journal of Air Transport Management, Vol. 87, 2020, p. 101852.
2. Johnson, W., and Silva, C., "NASA concept vehicles and the engineering of advanced air mobility aircraft," The Aeronautical Journal, Vol. 126, No. 1295, 2022, pp. 59–91.
3. Landgrebe A. J., 1972, The wake geometry of a hovering helicopter rotor and its influence on rotor performance. Journal of the American Helicopter Society, Vol. 17(4), pp. 3–15.
4. Leishman J.G.; Bagai A., 1991, Rotor wake visualization in low-speed forward flight. Paper 91-3232, AIAA 9th Applied Aerodynamics Conference, Baltimore, MD.
5. Sinibaldi G. and Marino, L., "Experimental analysis on the noise of propellers for small UAV," Appl. Acoust. 74(1), 79–88 (2013).
6. Intaratep, N., Alexander, W. N., Devenport, W. J., Grace, S. M. and Dropkin, A., "Experimental study of quadcopter acoustics and performance at static thrust conditions," AIAA Paper 2016-2873, 2016.
7. Zhou, W., Ning, Z., Li, H., Hu, H. An experimental investigation on rotor-to-rotor interactions of small UAV propellers. *Proceedings of the 35th AIAA Applied Aerodynamics Conference*, Denver, CO, USA, 5–9 June 2017; p. 3744. https: //doi.org/10.2514/6.2017-3744;
8. Shukla, D.; Komerath, N. Multirotor Drone Aerodynamic Interaction Investigation. *Drones*. 2018, 2, 43. https://doi.org/10.3390/ drones2040043.
9. Chen, M.; Cranes, D.; Hubner, J. Experimental investigation of rotor-wing interaction at low disk loading and low Reynolds number. In Proceedings of the AIAA Aviation 2019 Forum, 2019, p. 3034. https://doi.org/10.2514/6.2019-3034.
10. Lee, H., & Lee, D. J., "Rotor interactional effects on aerodynamic and noise characteristics of a small multirotor unmanned aerial vehicle," Physics of Fluids, 32(4), 2020.
11. Yin, J., De Gregorio, F., Petrosino, F., Rossignol, K-S, Schwarz, T., Cotte, B., Brouwer, H., Clero, F., Mortain, F., Reboul, G., Zanotti, A., Vigevano, L., Gibertini, G., Bernardini, G. Schmähl, M., Kaltenbach, H-K., Pagliaroli, T., Keßler, M., Barakos, G., Ragni, D., Testa, C.: Noise Radiation and Propagation for Multirotor System Configurations. In: Terms of Reference for the GARTEUR Action Group HC/AG-26, December 2021.
12. Rossignol, K.-S., Yin, J., Rottmann, L.: Investigation of Small-Scale Rotor Aeroacoustic in DLR's Acoustic Wind Tunnel Braunschweig, in 28th AIAA/CEAS Aeroacoustics 2022 Conference., Southampton, UK, 2022
13. Nargi, R.E., Candeloro, P., De Gregorio, F., Ceglia, G. and Pagliaroli T., (2023) Fluid-dynamic and aeroacoustic characterization of side-by-side rotor interaction, Aerospace 10 (10) (2023) 851. https://doi.org/10.3390/aerospace10100851
14. Zanotti, A. and D. Algarotti. 2022. Aerodynamic interaction between tandem overlapping propellers in eVTOL airplane mode flight condition. Aerospace Science and Technology 124: 107518.
15. Yin, J., De Gregorio, Rossignol, K.S., Rottmann, L., Ceglia, G., Reboul, G., Barakos, G., Qiao, G., Muth, M., Kessler, M., Visingardi, A., Barbarino, M., Petrosino, F., Zanotti, A., Oberti, N., Galimberti, L., Bernardini, G., Poggi, C., Abergo, L., Caccia, F., Guardone, A., Testa, C., Zaghi, S., "Acoustic and Aerodynamic Evaluation of DLR Small-scale Rotor Configurations Within GARTEUR AG26," 49th European Rotorcraft Forum (ERF), Bückeburg, Germany, September 5–7, 2023;
16. Raffel M., Willert C. E., Wereley S. T., and Kompenhans J. (2007) Particle Image Velocimetry - A Practical Guide, Springer-Verlag Berlin Heidelberg, 2nd edition doi: 10.1007/978-3-540-72308-0.
17. De Gregorio, F., Candeloro, P., Ceglia, G., Pagliaroli, T. Flow field and acoustic assessment of twin rotors in hover conditions. *XXXI AIVELA Annual Meeting*, Milan, IT, December 5-6, 2023;
18. Graftieaux L., Michard M. and Grosjean N. (2001) Combining PIV, POD and vortex identification algorithms for the study of unsteady turbulent swirling flows. Meas. Sci. Technol. 12 1422–1429.
19. De Gregorio F., Visingardi A. (2020) Vortex detection criteria assessment for PIV data in rotorcraft applications. Exp Fluids 61, 179. doi:10.1007/s00348-020-03012-7.
20. Pierce, A. D. (2019). *Acoustics: an introduction to its physical principles and applications.* Springer